Vitrification-Enabled Enhancement of Proton Conductivity in Hydrogen-Bonded Organic Frameworks

Linfeng Liang (jtcl@sxu.edu.cn)
Shanxi University
Feng-Fan Yang
Shanxi University
Xiao-Lu Wang
Shanxi University
Jiayue Tian
Zhengzhou University of Light Industry
Yin Yang
Shanxi University

Article

Keywords:

Posted Date: October 12th, 2023

DOI: https://doi.org/10.21203/rs.3.rs-3391011/v1

Additional Declarations: There is **NO** Competing Interest.

Vitrification-Enabled Enhancement of Proton Conductivity in Hydrogen-Bonded Organic Frameworks

Author Information

Feng-Fan Yang,[a] Xiao-Lu Wang,[a, b] Jiayue Tian,[c] Yang Yin,[a] Linfeng Liang[a*]

[a]Institute of Crystalline Materials, Shanxi University, Taiyuan 030006, Shanxi, China

[b]College of Chemistry, Taiyuan University of Technology, Taiyuan, 030024, China

[c]School of Materials and Chemical Engineering, Zhengzhou University of Light Industry, Zhengzhou,450001, China

Abstract

Hydrogen-bonded organic frameworks (HOFs) are versatile materials with potential applications in proton conduction. Traditional approaches involve incorporating humidity control to address grain boundary challenges for proton conduction. This study finds vitrification as an alternative strategy to eliminate grain boundary effect in HOFs by rapidly melt quenching the kinetically stable **HOF-SXU-8** to glassy state **HOF-SXU-8-g**. Notably, a remarkable enhancement in proton conductivity without humidity was achieved after vitrification, from 1.31×10^{-7} S cm^{-1} to 5.62×10^{-2} S cm^{-1} at 100°C. Long term stability test showed negligible performance degradation, and even at 30°C, the proton conductivity remained at high level of 1.2×10^{-2} S cm^{-1}. Molecule dynamics (MD) simulations and X-ray total scattering experiments reveal the **HOF-SXU-8-g** system is consisted of three kinds of clusters, i.e., 1,5-Naphthalenedisulfonic acid (1,5-NSA) anion clusters, N,N-dimethylformamide molecule clusters, and H^+-H_2O clusters. In which, the H^+ plays an important role to bridge these clusters and the high conductivity is mainly related to the H^+ on H_3O^+. ^{1}H magic angle spinning (MAS) solid-state nuclear magnetic resonance (NMR) revealed that the H^+ mobility was increased significantly after the transformation. These findings provide valuable insights for optimizing HOFs, enabling efficient proton conduction, and advancing energy conversion and storage devices.

Introduction

In recent years, hydrogen-bonded organic frameworks (HOFs) have attracted much attention as novel multifunctional materials due to their advantages such as easy synthesis, precise single-crystal structure, and low energy consumption in the regeneration process[1-5]. These frameworks offer potential applications in various fields, including catalysis[6-8], sensors[9-13] and gas adsorption[14-18]. Specifically, HOFs are believed to hold great potential in proton conduction due to their rich inherent hydrogen bonding networks. However, a major challenge in harnessing the full potential of HOFs as efficient proton conductors lies in the presence of inter-particle boundaries, which hinders the desired proton transport.

Conventionally, most studies have relied on the incorporation of guest molecules, such as water, to enhance the grain contacts and achieve high proton conductivity in HOFs[19-26], which is also common in other crystalline materials such as MOFs[27-33], COFs[34-41]. The guest molecules serve as mediators that facilitate proton transfer between the HOF particles. While this approach has shown promising results, it introduces practical limitations, particularly at elevated temperatures where managing humidity becomes cost-intensive and logistically challenging in fuel cell applications. With references to the elimination of grain boundaries in coordination polymers[42-51], vitrification is considered as one feasible method. Mason group[52] has done pioneering work and demonstrated that a desymmeterization strategy can be used to realize glass transitions of an alkylguanidinium sulfonate HOF. However, it is presumably that the entire HOF precursor is in a low energy state and the glassy material obtained does not exhibit significant proton conduction properties.

In this work, two single crystals, kinetically stable **HOF-SXU-8** with higher energy and thermodynamically stable **HOF-SXU-9** with lower energy were synthesized through liquid-phase diffusion method. **HOF-SXU-8** could undergo a vitrification transformation to glassy state **HOF-SXU-8-g** at around 110°C (Scheme 1). Following this vitrification transformation, the proton

conductivity of **HOF-SXU-8-g** without humidity at 100°C reached as high as 5.62 × 10^{-2} S cm^{-1}, while the conductivity for **HOF-SXU-8** is only 1.31 × 10^{-7} S cm^{-1}. Remarkably, even at 30°C, the proton conductivity of **HOF-SXU-8-g** maintained a quite high level of 1.2 × 10^{-2} S cm^{-1}. Furthermore, after a stability test of 16 hours, the performance of **HOF-SXU-8-g** remained almost unchanged. On the other hand, due to its thermodynamic stability and limited free volume, **HOF-SXU-9**, does not undergo such transition. ^{1}H MAS solid-state NMR revealed that the H^{+} mobility was increased significantly after the transformation.

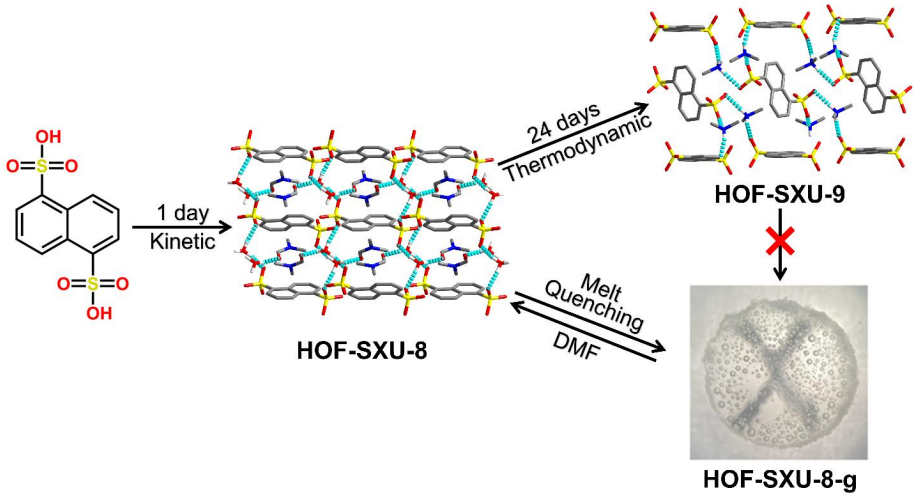

Scheme 1: Schematic representation of the synthesis of **HOF-SXU-8**, **HOF-SXU-9** and the vitrification transformation process to **HOF-SXU-8-g**. (Color code: C atom, gray; O atom, red; S atom, yellow; N atom, blue; H atom, white).

Results

Crystal structure descriptions of **HOF-SXU-8** and **HOF-SXU-9**

Single crystal X-ray analysis reveals that **HOF-SXU-8** crystallizes in the space group $P2_1/n$ (please see Table S1 for more details), with 1,5-NSA anion layers separated by DMF molecules. H_3O^{+} connects a continuous hydrogen bonding network capable of proton conduction by linking different 1,5-NSA anion layers and the DMF molecules (Fig. S1). Specifically, O(A) on H_3O^{+} forms one hydrogen bond with O(1A) from the upper layer of 1,5-NSA anion (O-H···O, 2.65 Å,

166.85°) and another hydrogen bond with O(2A) from the lower layer of 1,5-NSA anion (O-H···O, 2.65 Å, 152.37°), and one hydrogen bond with O(3A) on DMF (O-H···O, 2.44 Å, 161.86°) as depicted in Table S3. After soaking **HOF-SXU-8** in the mother solution for 4 days, the **HOF-SXU-8** crystals disappeared. Another 20 days later, thermodynamically stable colorless single crystals of **HOF-SXU-9** appeared in the space group $P2_1/c$ (please see Table S2 for more details). Dimethylamine cations in **HOF-SXU-9** link the differently oriented 1,5-NSA anion through two hydrogen bonds (Fig. S2 and Table S4). The purity of bulk crystalline **HOF-SXU-8** and **HOF-SXU-9** were confirmed through good accordance with the powder X-ray diffraction (PXRD) pattern simulated from the crystallographic information files, as shown in Fig. S3. Thermogravimetric (TG) analysis (Fig. S4) revealed that the kinetically stable **HOF-SXU-8** starts to lose weight at 100.26°C with a relatively low thermal stability. In contrast, the thermodynamically stable **HOF-SXU-9** can keep its structure intact to about 310°C. Above 310°C, 1,5-NSA anion starts to decompose, leading to the collapse of its skeleton. Overall, thermodynamically stable **HOF-SXU-9** exhibits higher thermal stability.

Crystal melting and glass formation

HOF-SXU-8 was heated at 110°C for 2h and then quenched rapidly to obtain **HOF-SXU-8-g** in glassy form (details please see supporting information section 2). To confirm the occurrence of vitrification, we used differential scanning calorimeter (DSC) to monitor the enthalpy response of the phase transition process (Fig. 1a). When the first heating cycle was applied, a heat absorption peak appeared at 100.26°C, the appearance of which was attributed to the phase transition of solid-liquid transformation occurring in the crystal. At the second heating cycle, the heat absorption peak disappeared, confirming the occurrence of vitrification, and the glass transition temperature T_g was calculated to be 20.66°C (Fig. 1b). PXRD (Fig. 1c) revealed that the characteristic peaks of crystalline **HOF-SXU-8** disappeared after melt quenching to **HOF-**

SXU-8-g accompanying by a new broad peak appeared, which is typical of glassy phase[47-50]. PXRD analyses conducted on the **HOF-SXU-9** sample after heated at 110°C for a duration of 2 hours have revealed that the distinctive peaks were still remained (Fig. S5), suggesting that the transformation of **HOF-SXU-9** into an amorphous or glassy state did not occur.

Scanning electron microscope (SEM) image clearly shows the presence of grain boundaries in the compressed **HOF-SXU-8** pellet. The morphology of the HOF crystals varies, with well-defined edges and grain boundaries clearly seen in Fig. 1e. While for **HOF-SXU-8-g**, the grain boundaries disappear and the whole material exists in homogeneous form (Fig. 1f). Optical photography is an effective way to observe changes in samples during heat treatment, thus allowing observation of processes such as sintering and melting. **HOF-SXU-8** pellet exhibited different degrees of transparency after processed at different temperatures[47, 53]. In Fig. 1g, where the sample is placed on the upper side of a printed “X”. The “X” is only visible after treated the pellet at 110°C for 2 hours and then cooled. Combining the results of the thermogravimetric analyses, it is clear that the change in transparency is due to the occurrence of vitrification.

In Fig. 1d, the C=O (1680 cm^{-1}) stretching vibration comes from the DMF structural unit and the O-H (3413 cm^{-1}) stretching vibration comes from the H_3O^+ structural unit, which is bound to the O-H bond after the formation of hydrogen bonding and the spectral peak broadens. These characteristic peaks are present in the Fourier transformed infrared (FTIR) spectra of both **HOF-SXU-8** and **HOF-SXU-8-g**, proving that the DMF structural unit and the hydrogen bonding network are still present in the structure after the vitrification process (Fig. 1d). Elemental analysis (Table S5) showed that the molecular formulas were $(1,5\text{-NSA})_{1.04}$ $(H_3O)_{2.25}$ $(DMF)_{2.2}$ for **HOF-SXU-8** and (1,5-NSA) $(H_3O)_{2.26}$ $(DMF)_{1.56}$ for **HOF-SXU-8-g**, with the difference related to the loss of approximately 30% DMF after glass formation. **HOF-SXU-8-g** was observed to re-crystallize (Fig. S6) back to **HOF-SXU-8** under heat treatment in DMF atmosphere, which is

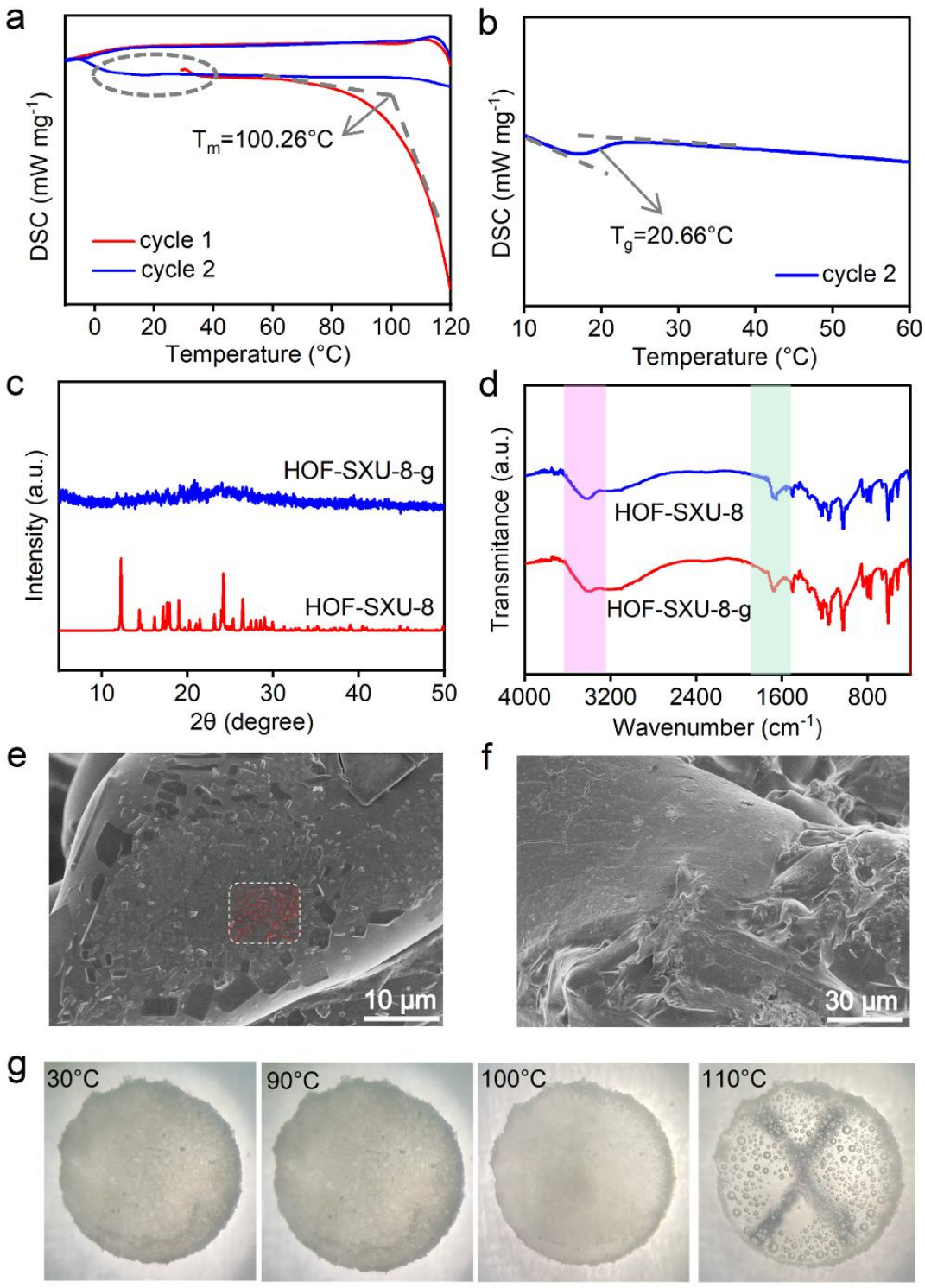

Fig. 1: a DSC scans of crystalline **HOF-SXU-8**; **b** Enlarged Figure of the circled part in Fig. 1a; **c** PXRD patterns of **HOF-SXU-8** and **HOF-SXU-8-g**; **d** FTIR spectra of **HOF-SXU-8** and **HOF-SXU-8-g**; **e** SEM image of the **HOF-SXU-8** pellet; **f** SEM image of the **HOF-SXU-8-g**; **g** Optical photographs of crystalline **HOF-SXU-8** after different temperature treatments. The sample was put on the mark "X" to assess the variation in transparency.

proved by the PXRD results (Fig. S7). However, no such re-crystallization was observed in the absence of DMF atmosphere, regardless of the same heat treatment temperature. This proves that the glass transformation is attributed to the partial release of structural DMF molecules, which is different from the complete guest molecules removal as previously reported by Mason's group[52].

Proton conduction properties

Electrochemical impedance spectroscopy (EIS) of **HOF-SXU-8**, **HOF-SXU-9** and **HOF-SXU-8-g** were measured without humidity at different temperatures. The conductivity values of **HOF-SXU-8** exhibited an increase from 3.40×10^{-9} S cm^{-1} at 30°C to 1.31×10^{-7} S cm^{-1} at 100°C (Fig. 2a and Fig. S8) with the crystalline phase of **HOF-SXU-8** remained throughout the measurements (Fig. S11). Crystalline structure of **HOF-SXU-9** was also maintained (Fig. S11) and the conductivity slightly increased from 4.15×10^{-9} S cm^{-1} at 30°C to 8.31×10^{-9} S cm^{-1} at 100°C (Fig. S9), which is ranked at a very low level[24, 54]. This phenomenon may be related to the strong hydrogen bonding network in the thermodynamically stable **HOF-SXU-9**.

Conductivity measurements of **HOF-SXU-8-g** revealed a high value of 1.02×10^{-2} S cm^{-1} at 30°C, and then increased slowly to 5.62×10^{-2} S cm^{-1} at 100°C (Fig. 2b and Fig. S10). The proton conductivity of **HOF-SXU-8-g** has been improved by about 5 orders of magnitude compared to single-crystalline **HOF-SXU-8**, making **HOF-SXU-8-g** a superior proton conductive material[20, 22, 23, 25, 55-57]. The Arrhenius plot (Fig. 2c) demonstrates different mechanisms of **HOF-SXU-8** and **HOF-SXU-8-g**: the activation energy of **HOF-SXU-8** was calculated to be 0.51 eV for the vehicular mechanism, while the activation energy value of **HOF-SXU-8-g** was 0.23 eV, which is typical for the Grotthuss mechanism[58]. In addition, **HOF-SXU-8-g** can maintain its superior proton conductivity up to 16 h at 100°C (Fig. 2d and Fig. S12) with performance kept

almost the same, revealing that the glassy **HOF-SXU-8-g** structure is well retained in this process.

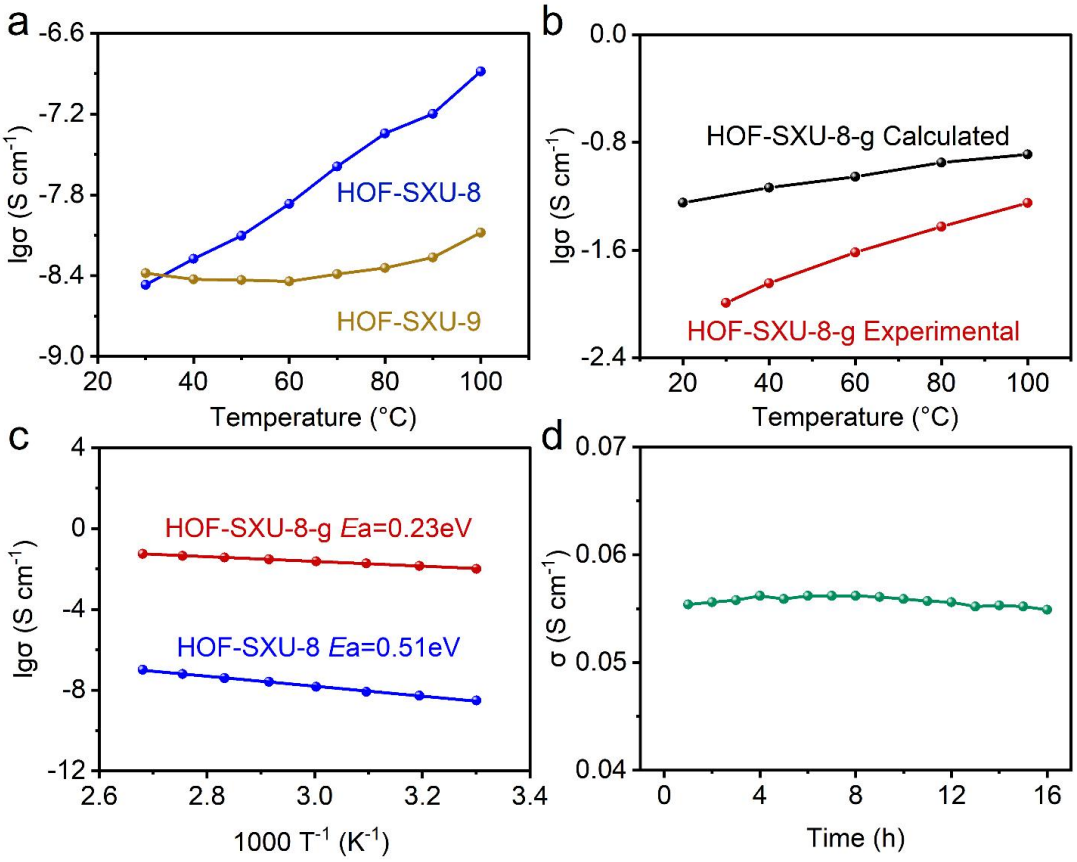

Fig. 2: a Proton conductivity of **HOF-SXU-8** and **HOF-SXU-9** with increasing temperature; **b** Experimental (red) and calculated (black) proton conductivity of **HOF-SXU-8-g** with increasing temperature; **c** Arrhenius plot of **HOF-SXU-8** and **HOF-SXU-8-g**; **d** Time-dependent proton conductivity of **HOF-SXU-8-g** performed at 100°C.

Simulation and Proton conduction mechanism

In order to probe the proton conduction mechanism, we performed MD simulations using LAMMPS 2022 software (details please refer to supporting information). An energy minimization procedure and an NVT ensemble simulation (T = 298 K, p = 1 bar, time = 1 ns) were employed to obtain equilibrated conformation (Fig. 3a). Further NVT ensemble simulation (15 ns, T = 298

K) and annealing procedure (5 ns, 298 K-873 K) were performed to assure that the above obtained system is stable.

The radial distribution functions (RDF) of 1,5-NSA anion-1,5-NSA anion, DMF-DMF have similar multiple peaks within 0.6 nm (Fig. 3c), suggesting that both 1,5-NSA anion and DMF spontaneous aggregated to clusters with a radius of 0.5-0.6 nm and exhibited a certain spatial distribution. The RDF of 1,5-NSA anion-DMF is low within 0.6 nm, indicating that the two clusters are mutually exclusive. Beyond 0.8 nm, it gradually converges to 1, indicating that the clusters are more uniformly dispersed with each other. Besides, there are significant interactions between the H_2O molecules to form clusters with radius of 0.4-0.5 nm, while no significant interactions between H_2O and 1,5-NSA anion, or between H_2O and DMF (Fig. 3d). Beyond 1.2 nm, the RDFs associated with H_2O converge to 1, indicating that the H_2O clusters are dispersed with other components of **HOF-SXU-8-g** (Fig. 3d). Similarly, the RDF between H^+ and H_2O (Fig. S14) is exceeded near 0.36 nm, suggesting that an indirect association is formed between H^+ relying on the H_2O molecule, while no significant H^+-1,5-NSA anion and H^+-DMF interaction were observed. In summary, the system are summarized by the following features: (1) the substances are divided into three kinds of clusters, i.e., 1,5-NSA anion clusters, DMF molecule clusters, and H^+-H_2O clusters, with the cluster radius of 0.4-0.6 nm; (2) the clusters were diffused with each other over medium and long distances (>0.8-1.2 nm). We also obtained the X-ray total scattering pattern of **HOF-SXU-8-g** and compared it with the simulated data based on the MD model (Fig. 3e). The experimental X-ray total scattering pattern of **HOF-SXU-8-g** agrees well with that of the simulated results, indicating that the structure of **HOF-SXU-8-g** is consistent with simulated **HOF-SXU-8-g**, further confirming the accuracy of our simulated **HOF-SXU-8-g** structure as discussed above.

The final equilibrated structure was then subjected to 1 ns equilibrium sampling, with the structure saved every 5 ps to form a trajectory and the interaction energy saved every 1 ps. The

electrostatic interaction energies and long-range non-bonding interaction energies between 1,5-NSA anion, DMF molecules, H^+, and H_2O were decomposed, and Fig. S15 demonstrates the interaction energies of each group as a percentage of the total interaction energy. 1,5-NSA anion-1,5-NSA anion, 1,5-NSA anion-H^+, DMF-DMF, H^+-H^+, and H^+-H_2O interactions occupied the top four proportion. 1,5-NSA anion-H_2O had a lower interaction energy (4%), whereas 1,5-NSA anion-H^+ (19.7%) and H^+-H_2O (8.8%) had higher interaction energies, so H^+ acted as a bridge connecting 1,5-NSA anion clusters to H_2O clusters, leading to the two types of clusters mixed and dispersed. Identically, 1,5-NSA anion-DMF has a lower interaction energy (0.9%), while the interaction energies of 1,5-NSA anion-H^+ and H^+-DMF account for 19.7% and 3.8%, respectively, thus H^+ also serves as a bridge between 1,5-NSA clusters and DMF clusters. In short, among the three original constituents of the **HOF-SXU-8-g** system, H^+ acts as a bridge between the clusters of the whole system.

The snapshot of the local structure in the middle period of simulation was drawn in Fig. 3b to display the rich hydrogen bonding. Hydrogen bonding analysis was carried out on the simulated trajectories to elucidate the contribution of different components. The number of hydrogen bonds generated by 1,5-NSA anion, DMF molecules, and the system averaged over different distances was analyzed (Fig. 3f). The hydrogen bonds formed by 1,5-NSA anion and DMF molecules in the system were distributed mainly at the distance range of 0.22-0.28 nm, and the number of hydrogen bonds formed by 1,5-NSA anion was significantly higher than that of DMF molecules. Thus, for this system, more hydrogen bonds can be formed in the same volume due to the release of DMF, which strengthens the hydrogen bonding network in the system and forms a glassy structure, and in turn would greatly enhance the proton conductivity of the glassy **HOF-SXU-8-g**.

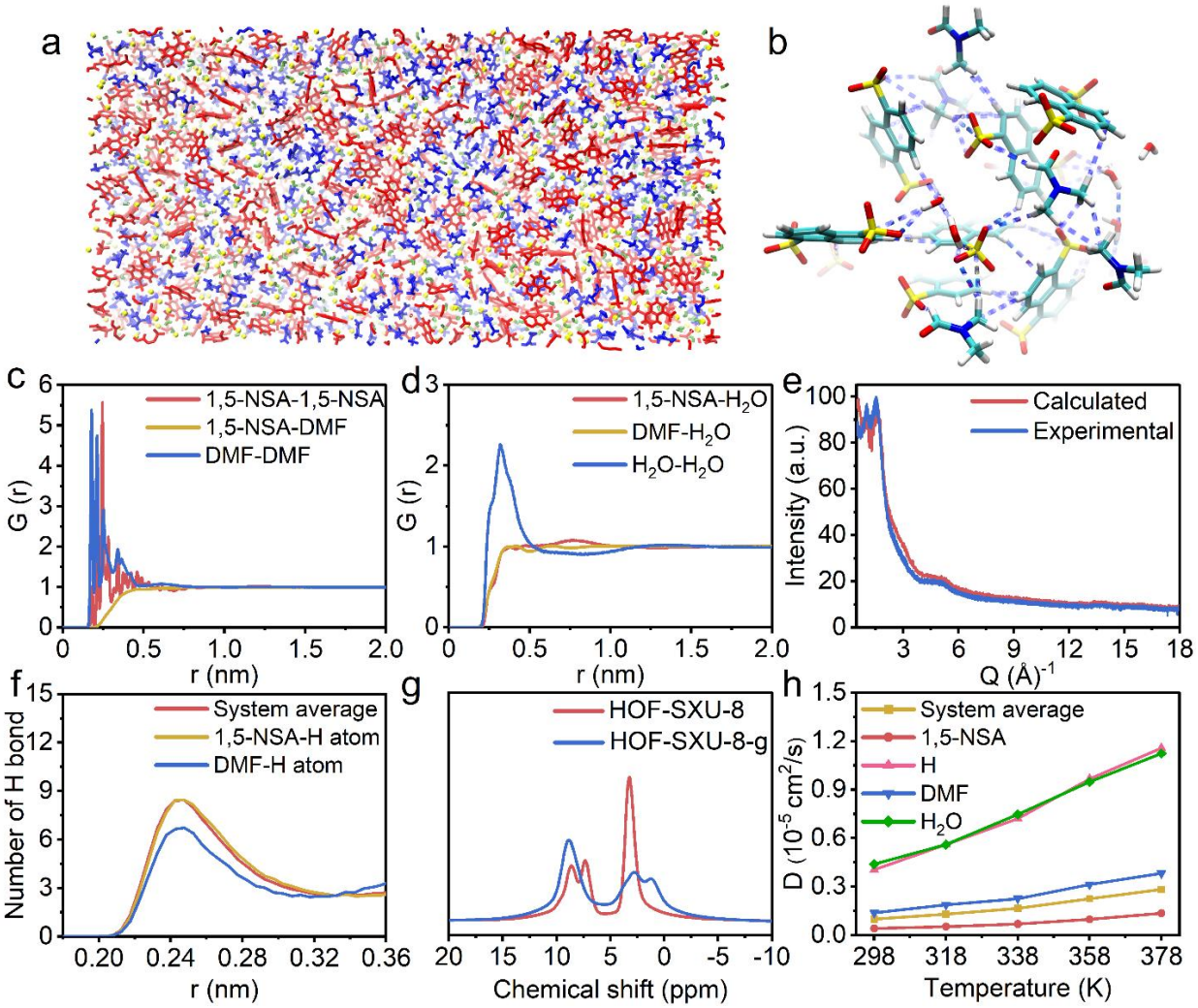

Fig. 3: a Structure diagram of simulated **HOF-SXU-8-g** (Cluster Color: 1,5-NSA anion, red; DMF molecule, blue; H^+, yellow; H_2O molecule, green); **b** Transient local structure of simulated **HOF-SXU-8-g** in MD simulation process (Color code: C atom, pale blue; O atom, red; S atom, yellow; N atom, blue; H atom, white); **c** RDFs associated with 1,5-NSA anion and DMF molecules; **d** RDFs associated with H_2O molecules; **e** X-ray total scattering pattern of **HOF-SXU-8-g** at room temperature (blue) compared with that calculated from MD simulations (red); **f** Distribution of the number of hydrogen bonds over distance; **g** ^1H MAS solid-state NMR spectra of **HOF-SXU-8** and **HOF-SXU-8-g** at room temperature; **h** Self-diffusion coefficients of different components from **HOF-SXU-8-g** at different temperatures.

The self-diffusion coefficients of different components in the simulated **HOF-SXU-8-g** increased with the increasing of temperature (Fig. 3h). The self-diffusion coefficients of H^+ and H_2O are the largest two among all species and are always closer at different temperatures, which also confirms the existence of H^+-H_2O clusters. The calculated conductivity values of the simulated

HOF-SXU-8-g system at different temperatures are shown in Fig. 2b. At 308 K and without an applied electric field, the conductivity is 6.41 × 10^{-2} S cm^{-1}, which is quite close to the experimentally obtained conductivity of 1.20 × 10^{-2} S cm^{-1}. Due to the huge difference in the self-diffusion coefficients between H^+ and 1,5-NSA anion, the main contribution to the electrical conductivity (90.7%) of the system comes from the diffusion of hydrogen ions (H^+-H_2O clusters) (Fig. 3h). Since the conductivity is mainly related to H^+ on H_3O^+, ^{1}H MAS solid-state NMR was utilized to study H^+ mobility (Fig. 3g). The peaks with chemical shifts of 5-10 ppm are attributed to H^+ on H_3O^+.The peak of H^+ on H_3O^+ of **HOF-SXU-8** is cleaved because H_3O^+ forms hydrogen bonds with 1,5-NSA between the layers and with the DMF molecule. While H^+ on H_3O^+ of **HOF-SXU-8-g** only exhibits one averaged single peak at 5-10 ppm because of its isotropic property after vitrification. It could also be deduced that after vitrification, the ease of movement of H^+ increases due to the peak intensity significantly increased (Fig. 3g), which further leads to the substantial increase in the proton conductivity.

Discussion

In summary, we have successfully prepared two hydrogen bonded organic frameworks: kinetically stable **HOF-SXU-8** and thermodynamically stable **HOF-SXU-9**, through controlling the reaction time. **HOF-SXU-8** could be transformed by rapidly melt quenching method at about 110°C to glassy state **HOF-SXU-8-g** triggered by partial loss of DMF molecules. **HOF-SXU-8-g** exhibits superior anhydrous proton conduction performance from 30°C to 100°C, with conductivity reaching as high as 5.62 × 10^{-2} S cm^{-1} and excellent stability. MD simulations and X-ray total scattering experiments reveal the **HOF-SXU-8-g** system can be divided into three kinds of clusters, i.e., 1,5-NSA anion, DMF molecule, and H^+-H_2O clusters. In which, the H^+ plays important role to bridge these clusters and the conductivity is mainly related to H^+ on H_3O^+. ^{1}H MAS solid-state NMR revealed that the H^+ mobility was increased significantly after the glass transformation. We believe that the glassy HOF will be a design well worth exploring in depth

and may open new avenues for obtaining safe and high-performance pure solid-state electrolytes.

Methods

Synthesis

All solvents and materials were purchased commercially and used without further purification. 1,5-NSA was purchased from Adamas-Beta. DMF and n-hexane were purchased from Tianjin Damao Chemical Reagent Factory.

Synthesis of **HOF-SXU-8**: 1,5-NSA (2.08 mmol, 600 mg) was dissolved in DMF (5 mL) in a 20 mL glass vial by ultrasound at 25°C. 1 mL of the above solution was then placed in a 20 mL glass vial and 2 mL hexane was added slowly. After 1 day, transparent **HOF-SXU-8** crystals were precipitated in the bottom of the glass vial. Crystallographic data for **HOF-SXU-8** has been deposited with the Cambridge Crystallographic Data Centre, CCDC, depository number 2292290.

Synthesis of **HOF-SXU-9**: The above obtained **HOF-SXU-8** was observed to disappear after 4 days of its appearance. Another 20 days later, thermodynamically stable crystals of **HOF-SXU-9** appeared in the bottom of the glass vial. Crystallographic data for the **HOF-SXU-9** has been deposited with the Cambridge Crystallographic Data Centre, CCDC, depository number 2292291.

Synthesis of **HOF-SXU-8-g**: **HOF-SXU-8-g** were obtained by rapid melt quenching of **HOF-SXU-8**. **HOF-SXU-8** crystals were ground to powder first and 15 mg of the powder was pressed into a pellet. The pressed **HOF-SXU-8** pellet was further heated in an oven at 110°C for 2h and then quickly quenched to obtain **HOF-SXU-8-g**.

Characterizations

TG was performed on a NETZSCH STA 449C thermal analyzer under nitrogen (N_2) atmosphere from 30 to 900°C at a rate of 10°C/min. T_g was determined by differential scanning calorimetry (DSC) (STA 404 C,Netzsch) and collected with a Netzsch DSC 200 F3 under N_2 atmosphere (Al crucible). The morphology of **HOF-SXU-8** and **HOF-SXU-8-g** were analyzed using SEM (Zeiss EVO 60 S). The changes of the samples after heat treatment were observed by optical and microscope. ^{1}H MAS Solid-state NMR was measured by the single pulse technique with a relaxation time of 3.00 s at a 8 kHz spinning rate at 28°C (^{1}H resonance frequency of 400.33 MHz). Elemental analyses (C, H, S and N) were performed in-house using an Elementar vario EL elemental analyzer.

X-ray characterization

The single crystal data were collected with a Rigaku XtaLab P200 diffractometer and a Dectris Pilatus 200K system at 302 K. The system was equipped with A MicroMax007 HF/VariMax rotating anode X-ray generator with confocal monochromatic Mo-Kα radiation. The collected data were solved and refined by full matrix least squares using SHELXL 2016/4. The phases of the synthesized crystals were identified using powder X-ray diffraction (PXRD) method. The PXRD experiments were performed on a Rigaku Ultima IV x-ray diffractometer at 40 kV and 40 mA with a scan rate of 1˚/min and a 2θ range of 5-50˚, and the diffractometer was equipped with a Cu sealed tube (λ = 1.5406 Å). Based on the single crystal diffraction data, simulated PXRD patterns were generated using Mercury 3.9 software.

Proton conductivity measurements

Proton conductivity was characterized through a two-probe method using a Solartron SI1260 Impedance / Gain-phase analyzer coupled with a Solartron 1287 dielectric interface. Before conductivity measurements, **HOF-SXU-8** and **HOF-SXU-9** samples were placed in a steel mold and pressed into pellets of 6 mm diameter and 1.5 mm thickness using a tablet press. For the

measurement of **HOF-SXU-8-g**, 100 mg **HOF-SXU-8** was first pressed into a 6 mm diameter pellet (pressure 10 MPa). **HOF-SXU-8** pellet was then put into a 2032 steel cell in a glove box filled with ultra pure Ar (H_2O and O_2 <1 ppm) and heated in an oven at 110°C for 2 hours to obtain **HOF-SXU-8-g** by rapidly melt quenching. All measurements in this work were performed under a stream of ultra-pure N_2 (>99.99%). The measurements were conducted in the frequency range from 0.5 Hz to 1 MHz with an input voltage amplitude value of 100 mV. The impedance values at each temperature were repeatedly measured after 30 minutes of equilibrium until the measured values keep stable. The resistance values were obtained by fitting the impedance profile using Zview software. The circuit equivalent used for fitting is as follows:

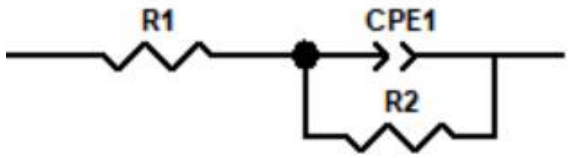

$$\sigma = {}^{l}/_{RS} \qquad (1)$$

$$\sigma T = A\exp({}^{-E_a}/_{k_B T}) \qquad (2)$$

R1 corresponds to the resistances of wire and electrode, while R2 accounts for the bulk resistance of the pellet. CPE1 denotes the nonideal capacitance corresponding to the bulk. The conductivity was calculated using equation (1), where σ is the conductivity (S cm^{-1}), *l* is the pellet thickness (cm), *S* is the solid electrolyte area (cm^2), and *R* is the bulk resistance of the pellet (R2 in the circuit equivalent) fitted by the equivalent circuit of the semicircle in Nyquist plot using zview software. The activation energy (E_a) of the material conductivity is estimated from equation (2), where *A* is the exponential prefactor, k_B is the Boltzmann constant, and *T* is experiment temperature.

X-ray total scattering measurements

HOF-SXU-8 sample was packed in a borosilicate capillary with a diameter of 0.7 mm， then in-situ heated at 110°C and quenched rapidly back to room temperature to obtain **HOF-SXU-8-g** in the borosilicate capillary. The X-ray total scattering data was collected on the Mythen-II detector over 115˚ covering the Q range up to 18 $Å^{-1}$ (21 keV; λ = 0.5921 Å). The wavelength, zero error and instrument contribution to the peak profile was determined using the line position and line shape standard NIST Si sample with the refined wavelength 0.5921 Å. For the experiment, an empty capillary was used as the background. The collected scattering data was applied absorption, background, and Compton scattering corrections then normalized to give the X-ray total scattering pattern.

Computational method

Molecular dynamics simulations were employed to study the material. The simulation is based on GAFF force field, and the force field parameters are obtained from quantum chemistry calculation and fitting, using m2seminario method. The long-range electrostatic term in the force field is calculated using Particle-Mesh-Ewald (PME) method, and the van der Waals interaction is calculated using Lennard-Jones potential (cutoff = 1.0 nm).

The simulation system contains 1440 naphthalenedisulfonic molecules, 2016 DMF molecules and 2880 water molecules, 62464 atoms in total.

Firstly, energy minimization procedure and an NVT ensemble simulation (T = 298 K, p = 1 bar, time = 1 ns) were employed to obtain a equilibrated and compressed conformation. After these processes, the system has a volume of 7.10×10^5 $Å^3$ and density of 1.26×10^3 kg/m^3.

Secondly, an NVT ensemble simulation (15 ns, T = 298 K) and an annealing procedure (5 ns, 298 K-873 K) were performed to assure that the system has been stable. The annealing procedure were performed in the protocol as below: 100 ps for each cycle, heat from 298 K to

873 K for 30 ps, keep temperature in 873 K for 30 ps, anneal from 873 K to 298 K in 5 ps, and keep temperature in 298 K for 35 ps, repeat the cycle for 50 times. After the above annealing procedure, the end structure kept the same as the start structure, which indicates that the system has been the stable structure already (Fig. S13).

A sampling for 1 ns was performed to the productive simulation, in which the timestep is 1 fs, trajectories were recorded every 5 ps, energies and properties were recorded every 1 ps.

References

1. P. Li, M. R. Ryder & J. F. Stoddart Hydrogen-Bonded Organic Frameworks: A Rising Class of Porous Molecular Materials. *Acc. Mater. Res.* **1,** 77-87 (2020).
2. B. Wang, R.-B. Lin, Z. Zhang, S. Xiang & B. Chen Hydrogen-Bonded Organic Frameworks as a Tunable Platform for Functional Materials. *J. Am. Chem. Soc.* **142,** 14399-14416 (2020).
3. J. Yang, et al. Porous hydrogen-bonded organic frameworks (HOFs): From design to potential applications. *Chem. Eng. J.* **399,** 125873 (2020).
4. Z.-J. Lin, S. A. R. Mahammed, T.-F. Liu & R. Cao Multifunctional Porous Hydrogen-Bonded Organic Frameworks: Current Status and Future Perspectives. *ACS Cent. Sci.* **8,** 1589-1608 (2022).
5. X. Song, et al. Design Rules of Hydrogen-Bonded Organic Frameworks with High Chemical and Thermal Stabilities. *J. Am. Chem. Soc.* **144,** 10663-10687 (2022).
6. B. Han, et al. Postsynthetic Metalation of a Robust Hydrogen-Bonded Organic Framework for Heterogeneous Catalysis. *J. Am. Chem. Soc.* **141,** 8737-8740 (2019).
7. J. Li, et al. In Situ Self-Assembly of Hydrogen-Bonded Organic Frameworks for Organic Photoredox Catalysis. *ACS Sustainable Chem. Eng.* **11,** 4389-4397 (2023).

8. Q. Zhou, Y. Guo & Y. Zhu Photocatalytic sacrificial H_2 evolution dominated by micropore-confined exciton transfer in hydrogen-bonded organic frameworks. *Nat. Catal.* **6,** 574-584 (2023).
9. I. Hisaki, et al. Acid Responsive Hydrogen-Bonded Organic Frameworks. *J. Am. Chem. Soc.* **141,** 2111-2121 (2019).
10. J. f. Feng, T. F. Liu & R. Cao An Electrochromic Hydrogen‐Bonded Organic Framework Film. *Angew. Chem. Int. Ed.* **59,** 22392-22396 (2020).
11. B. Wang, et al. Microporous Hydrogen-Bonded Organic Framework for Highly Efficient Turn-Up Fluorescent Sensing of Aniline. *J. Am. Chem. Soc.* **142,** 12478-12485 (2020).
12. C. Wang, et al. Ultrafine Silver Nanoparticle Encapsulated Porous Molecular Traps for Discriminative Photoelectrochemical Detection of Mustard Gas Simulants by Synergistic Size-Exclusion and Site-Specific Recognition. *Adv. Mater.* **34,** 2202287 (2022).
13. M. Jiang, et al. One-Component Artificial Gustatory System Based on Hydrogen-Bond Organic Framework for Discrimination of Versatile Analytes. *Adv. Funct. Mater.* **33,** 2300091 (2023).
14. Y. He, S. Xiang & B. Chen A Microporous Hydrogen-Bonded Organic Framework for Highly Selective C_2H_2/C_2H_4 Separation at Ambient Temperature. *J. Am. Chem. Soc.* **133,** 14570-14573 (2011).
15. Y.-L. Li, et al. Record Complexity in the Polycatenation of Three Porous Hydrogen-Bonded Organic Frameworks with Stepwise Adsorption Behaviors. *J. Am. Chem. Soc.* **142,** 7218-7224 (2020).
16. Y. Yang, et al. Ethylene/ethane separation in a stable hydrogen-bonded organic framework through a gating mechanism. *Nat. Chem.* **13,** 933-939 (2021).

17. P. Soleimani Abhari, et al. Recent progress in Gas Separation Platforms based on Hydrogen-Bonded Organic Frameworks (HOFs). *Inorg. Chem. Front.* DOI: 10.1039/D3QI00965C (2023).
18. Z. Yuan, et al. Sticked-Layer Strategy to a Flexible-Robust Hydrogen-Bonded Organic Framework for Efficient C_2H_2/CO_2 Separation. *CCS Chem.* 1-9 (2023).
19. L. Jiménez-García, et al. Phosphonated Hexaphenylbenzene: A Crystalline Proton Conductor. *Angew. Chem. Int. Ed.* **48,** 9951-9953 (2009).
20. A. Karmakar, et al. Hydrogen-Bonded Organic Frameworks (HOFs): A New Class of Porous Crystalline Proton-Conducting Materials. *Angew. Chem. Int. Ed.* **55,** 10667-10671 (2016).
21. W. Yang, et al. Microporous Diaminotriazine-Decorated Porphyrin-Based Hydrogen-Bonded Organic Framework: Permanent Porosity and Proton Conduction. *Cryst. Growth Des.* **16,** 5831-5835 (2016).
22. G. Xing, T. Yan, S. Das, T. Ben & S. Qiu Synthesis of Crystalline Porous Organic Salts with High Proton Conductivity. *Angew. Chem. Int. Ed.* **57,** 5345-5349 (2018).
23. Y. Wang, et al. Guest-tuned proton conductivity of a porphyrinylphosphonate-based hydrogen-bonded organic framework. *J. Mater. Chem. A* **9,** 2683-2688 (2021).
24. J.-Q. Qiao, S. Zuo, Z. Li & G. Li Latest progress in proton-conducting hydrogen-bonded organic frameworks. *Inorg. Chem. Front.* (2023).
25. Y. Sun, et al. Bio-Inspired Synthetic Hydrogen-Bonded Organic Frameworks for Efficient Proton Conduction. *Adv. Mater.* **35,** 2208625 (2023).
26. W.-W. Wu, et al. Controllable Synthesis and Ultrahigh Anisotropic Single-Crystal Proton Conduction of a Hydrogen-Bonded Organic Framework. *Chem. Mater.* **35,** 6549-6556 (2023).

27. W. J. Phang, et al. Superprotonic Conductivity of a UiO-66 Framework Functionalized with Sulfonic Acid Groups by Facile Postsynthetic Oxidation. *Angew. Chem. Int. Ed.* **54,** 5142-5146 (2015).
28. A.-L. Li, Q. Gao, J. Xu & X.-H. Bu Proton-conductive metal-organic frameworks: Recent advances and perspectives. *Coord. Chem. Rev.* **344,** 54-82 (2017).
29. F. Yang, et al. A flexible metal–organic framework with a high density of sulfonic acid sites for proton conduction. *Nat. Energy* **2,** 877-883 (2017).
30. S.-S. Bao, G. K. H. Shimizu & L.-M. Zheng Proton conductive metal phosphonate frameworks. *Coord. Chem. Rev.* **378,** 577-594 (2019).
31. Y. Tian, et al. Grafting Free Carboxylic Acid Groups onto the Pore Surface of 3D Porous Coordination Polymers for High Proton Conductivity. *Chem. Mater.* **31,** 8494-8503 (2019).
32. J. Chen, et al. Highly Efficient Proton Conduction in the Metal–Organic Framework Material MFM-300(Cr)·$SO_4(H_3O)_2$. *J. Am. Chem. Soc.* **144,** 11969-11974 (2022).
33. S.-S. Liu, et al. Sulfonic and phosphonic porous solids as proton conductors. *Coord. Chem. Rev.* **451,** 214241 (2022).
34. Y. Yang, et al. Combined Intrinsic and Extrinsic Proton Conduction in Robust Covalent Organic Frameworks for Hydrogen Fuel Cell Applications. *Angew. Chem. Int. Ed.* **59,** 3678-3684 (2020).
35. S. Yang, et al. Covalent Organic Frameworks with Irreversible Linkages via Reductive Cyclization of Imines. *J. Am. Chem. Soc.* **144,** 9827-9835 (2022).
36. B. Shi, et al. Short hydrogen-bond network confined on COF surfaces enables ultrahigh proton conductivity. *Nat. Commun.* **13,** 6666 (2022).
37. H. Ma, et al. Cationic Covalent Organic Frameworks: A Simple Platform of Anionic Exchange for Porosity Tuning and Proton Conduction. *J. Am. Chem. Soc.* **138,** 5897-5903 (2016).

38. Z. Lu, et al. Asymmetric Hydrophosphonylation of Imines to Construct Highly Stable Covalent Organic Frameworks with Efficient Intrinsic Proton Conductivity. *J. Am. Chem. Soc.* **144,** 9624-9633 (2022).
39. L. Liu, et al. Surface-Mediated Construction of an Ultrathin Free-Standing Covalent Organic Framework Membrane for Efficient Proton Conduction. *Angew. Chem. Int. Ed.* **60,** 14875-14880 (2021).
40. Z.-C. Guo, Z.-Q. Shi, X.-Y. Wang, Z.-F. Li & G. Li Proton conductive covalent organic frameworks. *Coord. Chem. Rev.* **422,** 213465 (2020).
41. C. Fan, et al. Scalable Fabrication of Crystalline COF Membranes from Amorphous Polymeric Membranes. *Angew. Chem. Int. Ed.* **60,** 18051-18058 (2021).
42. W. Xu, et al. High-Porosity Metal-Organic Framework Glasses. *Angew. Chem. Int. Ed.* **62,** e202300003 (2023).
43. T. Ogawa, et al. Coordination polymer glass from a protic ionic liquid: proton conductivity and mechanical properties as an electrolyte. *Chem. Sci.* **11,** 5175-5181 (2020).
44. R. S. K. Madsen, et al. Ultrahigh-field ^{67}Zn NMR reveals short-range disorder in zeolitic imidazolate framework glasses. *Science* **367,** 1473-1476 (2020).
45. N. Ma, S. Kosasang, A. Yoshida & S. Horike Proton-conductive coordination polymer glass for solid-state anhydrous proton batteries. *Chem. Sci.* **12,** 5818-5824 (2021).
46. N. Ma, et al. Photoexcited Anhydrous Proton Conductivity in Coordination Polymer Glass. *J. Am. Chem. Soc.* **145,** 9808-9814 (2023).
47. S. Li, et al. Mechanical Properties and Processing Techniques of Bulk Metal–Organic Framework Glasses. *J. Am. Chem. Soc.* **141,** 1027-1034 (2018).
48. Y. Feng, et al. Thermal treatment optimization of porous MOF glass and polymer for improving gas permeability and selectivity of mixed matrix membranes. *Chem. Eng. J.* **465,** 142873 (2023).

451 49. W. Chen, et al. Glass Formation of a Coordination Polymer Crystal for Enhanced Proton
452 Conductivity and Material Flexibility. *Angew. Chem. Int. Ed.* **55,** 5195-5200 (2016).
453 50. M.-Z. Chen, et al. Multi-stage Transformations of a Cluster-Based Metal-Organic
454 Framework: Perturbing Crystals to Glass-Forming Liquids that Re-Crystallize at High
455 Temperature. *Angew. Chem. Int. Ed.* **62,** e202305942 (2023).
456 51. T. D. Bennett, et al. Melt-Quenched Glasses of Metal-Organic Frameworks. *J. Am. Chem.*
457 *Soc.* **138,** 3484-92 (2016).
458 52. A. H. Slavney, et al. Liquid and Glass Phases of an Alkylguanidinium Sulfonate Hydrogen-
459 Bonded Organic Framework. *J. Am. Chem. Soc.* **144,** 11064-11068 (2022).
460 53. M. Stepniewska, M. B. Østergaard, C. Zhou & Y. Yue Towards large-size bulk ZIF-62
461 glasses via optimizing the melting conditions. *J. Non-Cryst. Solids* **530,** 119806 (2020).
462 54. S. C. Pal, D. Mukherjee, R. Sahoo, S. Mondal & M. C. Das Proton-Conducting Hydrogen-
463 Bonded Organic Frameworks. *ACS Energy Lett.* **6,** 4431-4453 (2021).
464 55. X.-L. Wang, et al. Boosting Proton Conductivity in Hydrogen-Bonded Organic Layers by
465 Modulating Embedded Guest Molecules. *Cryst. Growth Des.* **23,** 6221-6227 (2023).
466 56. X.-L. Wang, L. Liang, S. Dou & X.-M. Zhang Two-in-one tecton strategy to construct single
467 crystalline hydrogen-bonded organic framework with high proton conductivity above 100 °C.
468 *Sci. China Chem.* **66,** 2563-2568 (2023).
469 57. S. Chen, et al. Photo Responsive Electron and Proton Conductivity within a Hydrogen-
470 Bonded Organic Framework. *Angew. Chem. Int. Ed.* e202308418 (2023).
471 58. K.-D. Kreuer Proton Conductivity: Materials and Applications. *Chem. Mater.* **8,** 610-641
472 (1996).

473

474 Acknowledgements

475 This research was supported by National Natural Science Foundation of China (22001154).

Ethics declarations

Competing interests

The authors declare no competing financial interests.

Data Availability

The X-ray crystallographic coordinates for structure reported in this article have been deposited at the Cambridge Crystallographic Data Centre (CCDC), under deposition number CCDC 2292290 and 2292291. These data can be obtained free of charge from The Cambridge Crystallographic Data Centre via www.ccdc.cam.ac.uk/data_request/cif.

Supplementary Files

This is a list of supplementary files associated with this preprint. Click to download.

- SupportingInformation.pdf